Pressure-induced structural and electronic transitions, metallization, and enhanced visible-light responsiveness in layered rhenium disulphide

Pei Wang,[1,2] Yonggang Wang,[3] Jingyu Qu,[1,4] Qiang Zhu,[1,*] Wenge Yang,[3] Jinlong Zhu,[1,3] Liping Wang,[1,†] Weiwei Zhang,[4] Duanwei He,[2] and Yusheng Zhao[1,5,‡]

[1]*High Pressure Science and Engineering Center, University of Nevada, Las Vegas, Las Vegas, Nevada 89154, USA*
[2]*Institute of Atomic and Molecular Physics, Sichuan University, Chengdu 610065, China*
[3]*Center for High Pressure Science and Technology Advanced Research (HPSTAR), Beijing 100094, China*
[4]*Department of Applied Physics, China Agricultural University, Beijing 100080, China*
[5]*Department of Physics, Southern University of Science and Technology, Shenzhen 518055, China*

Triclinic rhenium disulphide (ReS_2) is a promising candidate for postsilicon electronics because of its unique optic-electronic properties. The electrical and optical properties of ReS_2 under high pressure, however, remain unclear. Here we present a joint experimental and theoretical study on the structure, electronic, and vibrational properties, and visible-light responses of ReS_2 up to 50 GPa. There is a direct-to-indirect band-gap transition in $1T$-ReS_2 under low-pressure regime up to 5 GPa. Upon further compression, $1T$-ReS_2 undergoes a structural transition to distorted-$1T'$ phase at 7.7 GPa, followed by the isostructural metallization at 38.5 GPa. Both *in situ* Raman spectrum and electronic structure analysis reveal that interlayer sulfur–sulfur interaction is greatly enhanced during compression, leading to the remarkable modifications on the electronic properties observed in our subsequent experimental measurements, such as band-gap closure and enhanced photoresponsiveness. This study demonstrates the critical role of pressure in tuning materials properties and the potential usage of layered ReS_2 for pressure-responsive optoelectronic applications.

I. INTRODUCTION

In recent years, the layered transition-metal dichalcogenides (TMDs) (MX_2, where M denotes metal atoms Mo, W, Re, etc., and X denotes S, Se, and Te), as a new class of quasi-two-dimensional (2D) materials beyond graphene, have attracted tremendous interest [1–7]. Atomically thin monolayer TMDs, prepared by mechanical exfoliation or chemical vapor transports, have been found to exhibit a variety of exotic transport properties such as quantum spin Hall effect [8], charge-density waves [9–11], and superconductivity [12–14], thus enabling many potential applications.

In the crystal structures of TMDs, metal atoms (M) are sandwiched between graphenelike layers of chalcogen atoms (X), forming a layered structure with MX_2 stoichiometry. The metal atoms can either occupy the original prismatic holes between chalcogen layers as H phase, or the octahedral holes as T phase. The most common form in TMDs is the H phase, whereas T phases are reported to be metastable. However, ReS_2 is an exception, in which the most stable form under ambient condition is a distorted $1T$ phase with triclinic symmetry, due to the pronounced Peierls distortion [15–20]. Unlike in other TMDs, Peierls distortion of the $1T$ structure of ReS_2 weakens the coupling interaction, which in turn hinders S-Re-S layers from stacking orderly and

minimizes the interlayer overlap of wave functions to open a band gap ($\sim$1.4 eV) [15] in the bulk ReS_2. Moreover, it has been proposed that ReS_2 holds a direct band gap in both bulk and monolayer forms, whereas most TMDs undergo a transition from indirect to direct band-gap semiconductor when reduced from bulk to monolayer. This robust direct band-gap feature makes ReS_2 very promising for practical applications [15,17,21,22].

High pressure has been proved an effective means to tune the physical properties of materials via modifying the atomic and electronic structures [23–28]. For example, the pressure response of MoS_2 (the most common one in the TMD family) has been widely investigated. Nayak *et al.* reported an electronic transition from a semiconducting to metallic state at $\sim$19 GPa in MoS_2 due to pressure-induced lattice distortion [25]. In addition to the bulk form, pressure is also able to control the band structure and optoelectronic properties of monolayered MoS_2. Bandaru *et al.* showed a pressure-induced isostructural hexagonal distortion to a $2H_a$-hexagonal $P6_3/mmc$ phase in MoS_2 around 26 GPa [28]. Going to higher pressure, Chi *et al.* observed the metallization (60 GPa) [23], and eventually the emergence of superconductivity (90 GPa) in pristine $2H$-MoS_2 [14]. Remarkably, the superconductivity transition temperature T_c reached up to 12 K under substantial compression [14]. The similar pressure-induced semiconductor-to-metal transition has also been found in $MoSe_2$ [24], WS_2 [26,27], and VS_2 [29].

Despite the growing studies on MX_2, the high-pressure behavior of ReS_2 remained largely unexplored until recently [20,30]. Hou *et al.* reported that ReS_2 undergoes a phase

*qiang.zhu@unlv.edu
†liping.wang@unlv.edu
‡zhaoys@sustc.edu.cn

transition at about 10.5 GPa based on x-ray diffraction (XRD) patterns analysis [30]. Unfortunately, the crystal structure of high-pressure phase could not be determined due to insufficient quality of XRD data. This puzzling high-pressure phase was further studied in a theoretical work, which revealed that multi-layered ReS_2 would undergo a structural transition to another P-1 phase (denoted as distorted-1T' hereafter), followed by a sluggish semiconducting to metallic (S-M) transition upon continuous compression [20]. However, the inadequate quality of the experimental diffraction data prevented convincing agreement between experiment and theory. More interestingly, there have been growing disputes regarding the claimed direct band gap in bulk ReS_2 in previous studies [15–22]. Recent pho-toluminescence (PL) and reflectance spectrum experiments at ambient conditions indicated that multilayer ReS_2 possesses an indirect optical gap at 1.40 eV [31]. If ReS_2 is indeed the indi-rect band-gap semiconductor, how will its electronic structure respond to pressure? Yan *et al.* made the first step in a recent study, in which they reported an intriguing indirect-indirect band-gap transition at 2.7 GPa by both high-pressure PL and *ab initio* calculations [32]. However, systematic study in a wider pressure range and detailed optoelectronic properties charac-terization upon compression are still lacking. This motivated us to perform a comprehensive study to address these challenges.

In this paper, combining *in situ* synchrotron XRD, Raman scattering, electrical transport study, visible-light-response measurements, and *ab initio* calculations, we have systemati-cally investigated crystal structures, metallization, vibrational response, and photocurrents of ReS_2 at pressures up to 50 GPa. The high-pressure ReS_2 phase has been predicted from *ab initio* calculation and further confirmed by the experimental XRD data. Both experiment and calculation suggest that ReS_2 undergoes a distorted-1T to distorted-1T' phase transition at $\sim$7.7 GPa and a further S-M transition at $\sim$38.5 GPa. The photoresponsiveness of ReS_2 polycrystalline samples contin-uously increases due to the structural modification under high pressure.

II. EXPERIMENTAL AND COMPUTATIONAL DETAILS

A. *In situ* high-pressure characterizations

Powder- and single-crystal ReS_2 samples were purchased from Alfa Aesar and 2D Semiconductors, respectively. High-pressure *in situ* powder XRD experiments were carried out by use of a symmetric diamond-anvil cell (DAC) with a culet size of 300 μm at 16-IDB of the High Pressure Collaborative Access Team (HPCAT), Advanced Photon Source (APS), Argonne National Laboratory (ANL) using a monochromatic x-ray beam with a wavelength of 0.4066 Å and 5 μm in diameter in size. Powder ReS_2 samples were loaded into a preindented rhenium gasket hole of 170 μm in diameter for XRD and Raman spectroscopy experiments, while the pressure
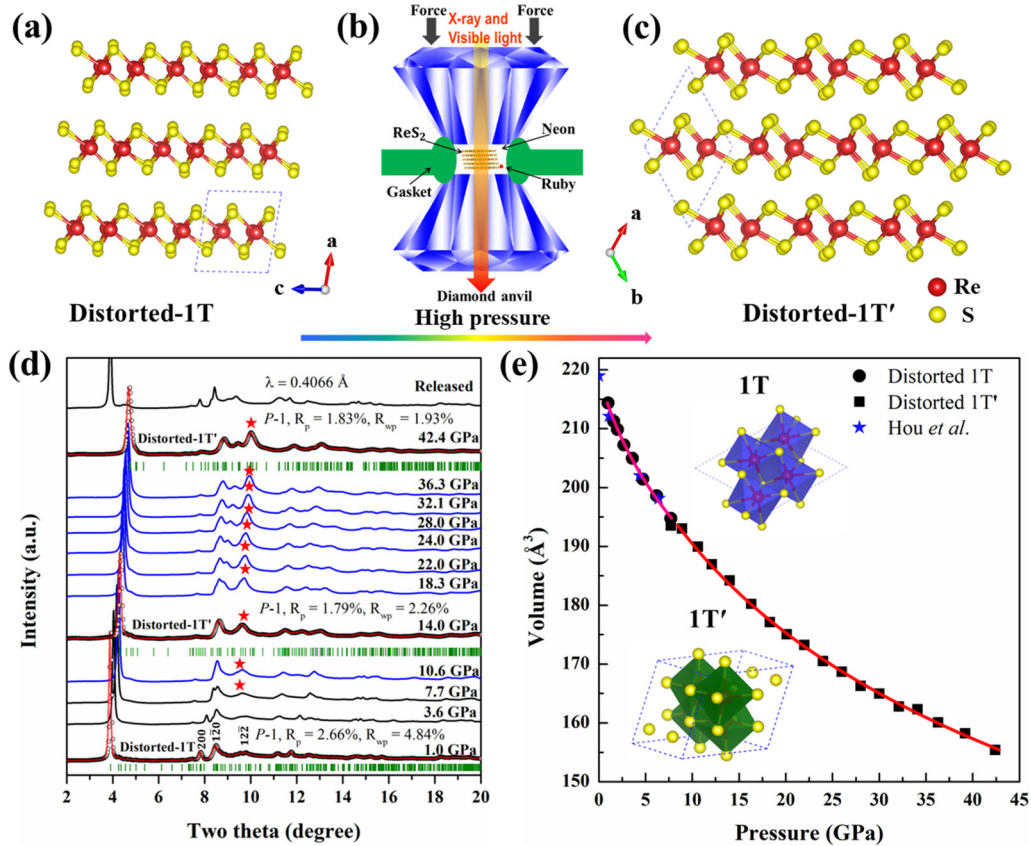

FIG. 1. Structure details, synchrotron XRD patterns, and pressure dependence of the unit-cell volume of ReS_2. (a) The cross-section illustration of layered distorted-1T ReS_2. (b) Schematic diagram of the high-pressure diamond-anvil cell setup. (c) The cross-section illustration of layered distorted-1T' ReS_2. (d) Selected XRD patterns of ReS_2 under high pressure. Red stars marking the diffraction peak from distorted 1T'. (e) The volume data of both phases of ReS_2 as function of pressure fitted by third-order Birch-Murnaghan equation of state.

was determined using ruby-fluorescence method and neon was used as the pressure-transmitting medium [33]. XRD patterns were collected by a PILATUS area detector and integrated into one-dimensional profile with the FIT2D program [34]. Structure refinements were performed using the Pawley method [35]. High-pressure electrical resistance (ER) was measured using a quasi-four-probe resistance measurement system consisting of a Keithley 6221 current source, a 2182A nanovoltmeter, and 7001 voltage/current switch system in a DAC and a cubic large-volume press (LVP) [36–38]. Photocurrent measurements of powder and single-crystal samples were performed using an Autolab PGSTAT128N workstation to keep track of the current-time data [38]. A 20-W incandescent lamp was chosen as the illumination source (~ 2 W/cm^2 on the sample). Dark current at the μA level was produced by applying a constant voltage, which varies from 0.002 to 0.3 V at a given pressure point (for example, 0.3 V at 4.7 GPa and 0.002 V at 39.3 GPa, respectively) owing to the changing of ER along the loading pressure [38].

B. First-principles calculations

The search for high-pressure structures was carried out with variable-cell structure prediction simulations using the evolutionary algorithm USPEX [39–41]. All structures were locally optimized using the density-functional theory method within the generalized gradient approximation (GGA) combining with the VASP package [42]. The all-electron projector augmented wave method was adopted with a plane-wave kinetic energy cutoff of 500 eV for all calculations [43]. For the band-structure calculations of bulk ReS$_2$, a set of $16 \times 16 \times 16$ k-mesh samplings was employed for Brillouin-zone integration. The convergence criterion of self-consistent-field calculations for ionic relaxations was set to 10^{-5} eV for the total energy. All unit cells and atomic positions were optimized until the atomic forces were less than $\sim$0.01 eV/Å. Pressures on the lattice unit cell for the convergence criterion of relaxation were reduced to values less than 0.02 GPa and the Hellman-Feynman forces on the ions were less than 0.001 eV/Å.

III. RESULTS AND DISCUSSION

A. *In situ* synchrotron XRD patterns and structural transition

At ambient condition, ReS$_2$ adopts a distorted CdCl$_2$-type layered structure with triclinic symmetry (space group P-1) [44,45]. As shown in Fig. 1(a), in each layer sulfur atoms form an octahedral coordination around rhenium atoms. Figure 1(b) shows the *in situ* high-pressure synchrotron XRD experimental setup in DAC. By sharing the edges, [ReS$_6$] octahedra are packed together in the bc plane, forming the ReS$_2$ monolayer perpendicular to the a axis. In the unit cell there is only one S-Re-S sandwich. This stacking mode is known as distorted-1T ReS$_2$. Due to the Peierls distortion, Re atoms dimerize each other to form the zigzag line of parallelogram-shaped Re$_4$ clusters (Figs. S1 and S2 in the Supplemental Material) [46], which gives the composition of Re$_4$S$_8$ in the unit cell.

Figure 1(d) shows the selected XRD patterns of ReS$_2$ under high pressure. Upon compression, while all peaks shifted to larger 2θ (smaller d spacing), the (200) peak representing the

interlayer spacing along the a axis moved faster to smaller d spacing and merged with (1$\bar{2}$0) peak into a single broad feature between 7.7 and 18.3 GPa. The more rapid shift of the (200) peak suggests that the a axis is more compressible than the b and c axes owing to the interlayer decoupling interactions (Fig. S3) [46]. There appeared a peak (marked with red star) at the left shoulder of the (12$\bar{2}$) peak at 7.7 GPa, whose intensity increased with increasing pressure during subsequent compression to 42.4 GPa. A phase transition is hence inferred to have occurred at 7.7 GPa or a lower value due to the sluggish kinetics of the phase transformation.

From the XRD profile, the phase looks similar to the high-pressure phase previously reported by Hou *et al.* [30]. The phase, i.e., the distorted-1T' phase, was resolved to have a triclinic structure with the same space group of P-1 and 12 atoms in the unit cell in a recent theoretical study [see Fig. 1(c)] [20]. Indeed, our *ab initio* structure search also yielded the same structure. More importantly, the high-quality synchrotron XRD data with more intensive peaks in the current study allowed us to perform a better comparison with theoretical prediction [see Fig. 1(d) and Fig. S4] [46]. We therefore conclude that the distorted-1T' phase is the high-pressure phase observed in our experiment. In distorted-1T', all Re atoms
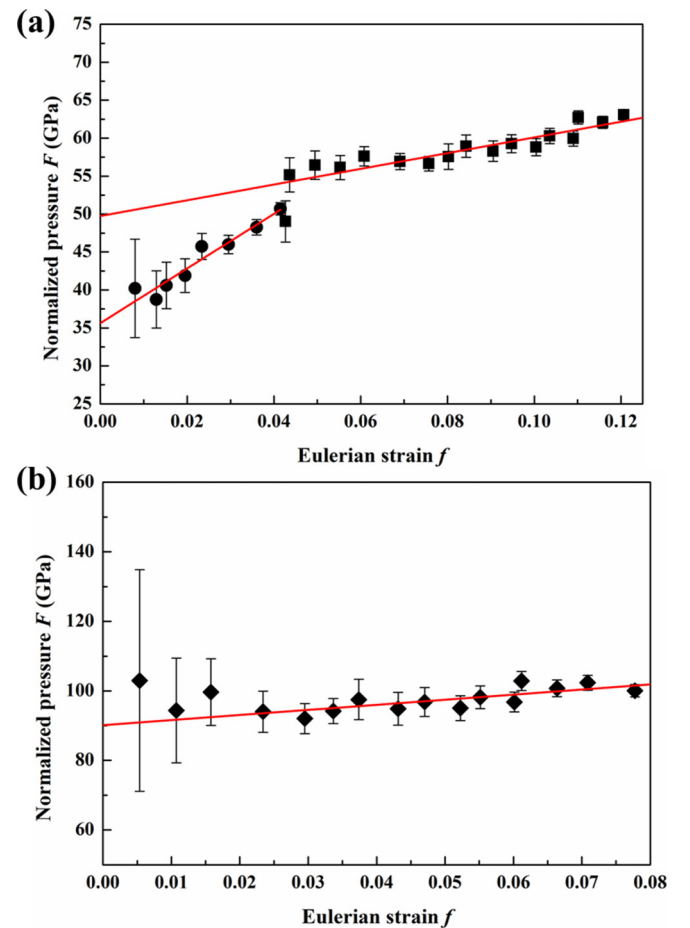

FIG. 2. Normalized pressure F vs Eulerian strain f. (a) F and f derived with reference volumes at ambient pressure (V_0) from BM-EoS for both phases. (b) F and f calculated using the reference pressure of 8.9 GPa for 1T' phase. Solid lines in both plots are linear fits using Eq. (4).

sharing the same (x, y) coordinates form different S-Re-S triple layer packing [Fig. 1(c)]. To minimize the interlayer S$\cdots$S repulsion, the angles between each sandwich of distorted-$1T'$ phase are more contorted than in $1T$-ReS$_2$. According to our calculation, the phase transition between $1T$ and distorted-$1T'$ is expected to take place at or near 3.1 GPa (Fig. S5) [46], which is in qualitative agreement with the experimental observations.

The crystal structure of distorted-$1T'$ ReS$_2$ from prediction was then used for further Pawley refinement (see Table S1) [46]. By fitting the P-V data to a third-order Birch-Murnaghan equation of state (BM-EoS) as shown in Fig. 1(e) [47],

$$P = \frac{3}{2} B_0 \left[\left(\frac{V}{V_0} \right)^{-7/3} - \left(\frac{V}{V_0} \right)^{-5/3} \right] \left\{ 1 + \frac{3}{4}(B_0' - 4) \right.$$
$$\left. \times \left[\left(\frac{V}{V_0} \right)^{-2/3} - 1 \right] \right\}, \tag{1}$$

where B_0 is the bulk modulus at ambient condition, and B_0' is the pressure derivative of B_0. We obtained bulk modulus $B_0 = 35.6 \pm 5.2$ GPa with $B_0' = 10.8 \pm 2.4$ and $V_0 = 219.49 \pm 0.81$ Å^3 for distorted-$1T$ phase, and $B_0 = 49 \pm 10$ GPa with $B_0' = 5.4 \pm 0.7$ and $V_0 = 218.83 \pm 3.65$ Å^3 for distorted-$1T'$

phase, respectively. Values of bulk modulus and its pressure derivative for distorted-$1T$-ReS$_2$ are substantially different from those in previous study [30]. To verify the quality of the BM-EoS fits, we converted P-V data to the Eulerian strain f and the corresponding normalized pressure F using V_0s from BM-EoS analyses for each respective phase according to the following formula [48–51]:

$$F = P[3f(1 + 2f)^{5/2}]^{-1}, \tag{2}$$

$$f = \frac{1}{2} \left[\left(\frac{V}{V_0} \right)^{-2/3} - 1 \right]. \tag{3}$$

The linear relationship between F and f is described as

$$F = B_0 + [3B_0(B_0' - 4)f]/2, \tag{4}$$

where B_0 is the bulk modulus at ambient pressure, and B_0' is the pressure derivative. Unlike in simple P-V plot, F-f data show a clear change in slope [Fig. 2(a)], indicating a change in mechanical performances likely associated with a polymorphic phase transformation [50]. The maximum change in slope is between Eulerian strain values of 0.030–0.050 corresponding to pressure values of 4.7–10.6 GPa. Linear regressions based on
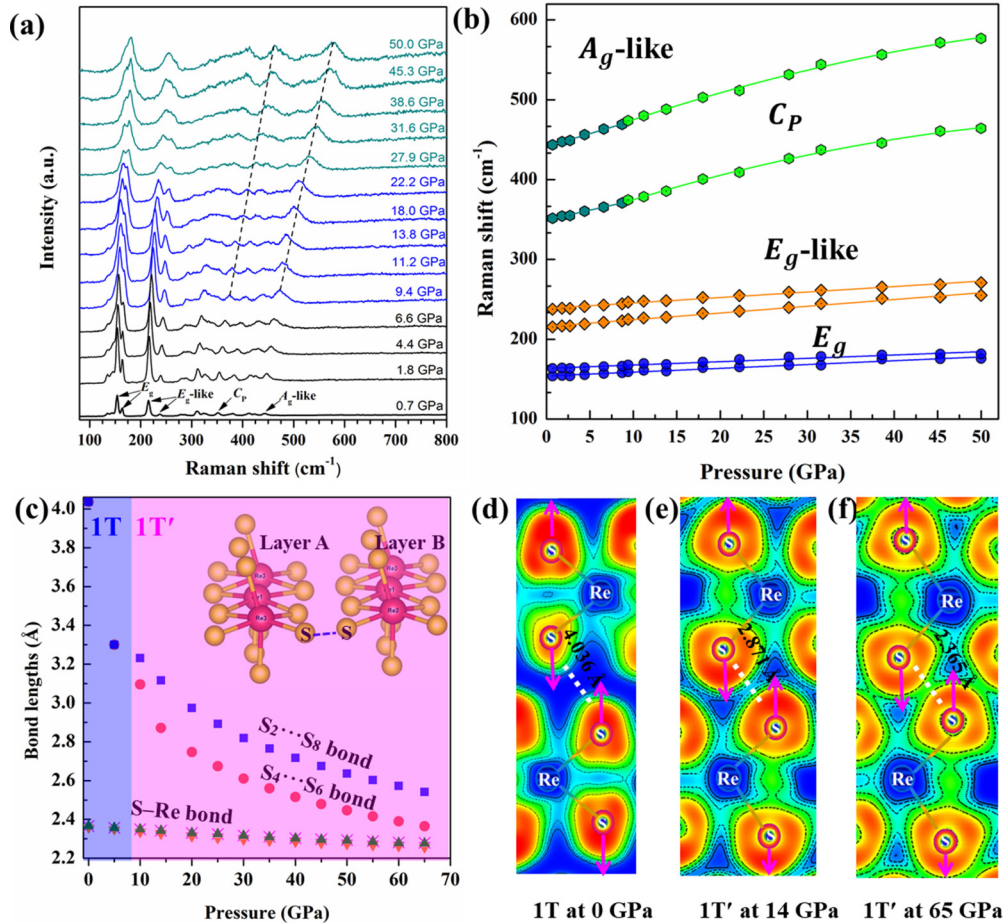

FIG. 3. Raman spectra results of ReS$_2$ under high pressure. (a) At room temperature and various pressures up to 50 GPa. The prominent modes E_g, E_g-like, C_p, and A_g-like are indicated by arrows. (b) The evolution of the most prominent Raman peaks of ReS$_2$ as a function of pressure. (c) The calculated bond lengths in $1T$ phase and $1T'$ phase ReS$_2$ as a function of pressure. Inset shows the shortest S–S bond between layers. (d)–(f) The key out-of-plane phonon mode A_g-like is shown in ELF profiles.

Eq. (4) to two sets of F-f data yield $B_0 = 35.6 \pm 1$ GPa with $B_0' = 10.7 \pm 0.8$ for the $1T$ phase and $B_0 = 49.8 \pm 1.1$ GPa with $B_0' = 5.4 \pm 0.2$ for the $1T'$ phase, all in good agreement with the result from BM-EoS fitting. It should be noted that the B_0 and B_0' obtained for the $1T'$ phase in the present study are for a hypothetical state of the unquenchable $1T'$ phase. From the linear fit to F-f data between 8.9 to 42.4 GPa (i.e., pure $1T'$ phase) calculated by using the measured unit-cell volume at 8.9 GPa as reference [51], we obtained a bulk modulus of 90.1 ± 2.2 GPa and a pressure derivative of 5.1 ± 0.3 for $1T'$ phase at 8.9 GPa [Fig. 2(b)]. The structural changes in both phases upon compression are highly anisotropic, as evidenced by the relationship between the lattice parameters and pressure (Fig. S3) [46]. The a axis along the layering direction is more compressible than the b axis and c axis owing to weaker interlayer coupling forces.

B. Raman spectra and evolution of S-S interaction under pressure

The phase transition from $1T$ to $1T'$ is also supported by the *in situ* Raman data [Fig. 3(a)]. The Raman spectroscopy revealed a large number (18) of vibrational modes for $1T$-ReS_2 due to its low lattice symmetry [18]. Most Raman-active modes undergo subtle changes under compression, except the discontinuous changes in A_g-like (438 cm^{-1}) and C_p (377.9 cm^{-1}) at 9.4 GPa [Fig. 3(a)]. Figure 3(b) shows the pressure-induced evolution for the most prominent Raman peaks in bulk ReS_2. The low-frequency Raman peaks (153.1, 163.6, 217.2, and 237.2 cm^{-1}) due to Re vibration are less sensitive to hydrostatic pressure when compared to other TMDs owing to decoupled vibration in ReS_2. The pressure dependence of the low vibrational frequencies follows almost linear behavior, which indicates nearly identical Re vibration in both $1T$ and $1T'$ phases. However, the slopes of C_p (377.9 cm^{-1}) and A_g-like (438 cm^{-1}) are significantly greater than those of the E_g-like modes. According to Ref [18], A_g-like mode is assigned to the out-of-plane S vibrations located at 438 cm^{-1} (a surface mode), while C_p mode simply represents the in-plane and out-of-plane coupled mode of Re and S atoms. The distinct features above 250 cm^{-1} are mainly contributed by intensive S-atom motions, which account for the layer sliding and continuously increasing interlayer S$\cdots$S interaction [18,23–27]. Indeed, the enhanced S$\cdots$S interaction is also evident from the evolution of S-S interlayer distances, which dropped significantly from 4.036 Å at ambient pressure to 2.365 Å at 65 GPa [Figs. 3(c) and 3(f)]. For reference, the van der Waals (vdW) radii for sulfur are typically 1.80 Å, while the covalent radii are 1.05 Å. This monotonic decrease suggests that S-S interaction undergoes a transition from vdW-like to covalentlike bonding. Compared to the S-S interactions in pyrite FeS_2, in which the S–S covalent bonds are less compressible than Fe–S bonds, the S-S distance in ReS_2 decreases much faster than Re–S bond length with increasing pressure due to the weak interlayer interaction. After formation of covalentlike bonding of S–S at high pressure, the contraction of S-S distance starts to slow down and the coupled librational and stretching motions of S–S dimer could be split into A_g-like mode and C_p [52,53]. To further understand the chemical bonding, we also performed the calculations on electron localization function

(ELF) [54]. Clearly shown in Figs. 3(d)–3(f), the significant ELF accumulation between S-S already appeared at 14 GPa, confirming the formation of S–S bonds as well.

C. *In situ* resistance measurements

To better understand the electronic properties of ReS_2 at high pressure, we performed *in situ* resistance (R) measurements using quasi-four-probe method in DAC and LVP (Figs. S6 and S7) [46]. Figures 4(a)–4(d) show the electrical resistance as a function of pressure and temperature (T). Upon compression, the resistance value dropped dramatically with increasing pressure, at least by four orders of magnitude, to a stable value of less than ~1 Ω at about 45.7 GPa, suggesting a semiconductor to metal transition. *In situ* temperature-dependent resistance measurements [see Figs. 4(b)–4(d)] further confirmed the metallic behavior above 38.5 GPa. Bulk ReS_2 displays the classical semiconducting behavior at low pressures as the temperature coefficient of resistance (dR/dT) is negative at 12.3 GPa [Fig. 4(b)]. At 17.6 GPa, the temperature-resistance curve reflects a semiconducting behavior at the low-temperature region and a metallic one above 200 K with a positive dR/dT [20,23–27]. A full metallization of ReS_2 was realized at 38.5 GPa as a positive dR/dT remained throughout all temperatures. The theoretical calculation predicts the band-gap closure of ReS_2 at ~40 GPa [Fig. 4(e)], in excellent agreement with the experimental results.
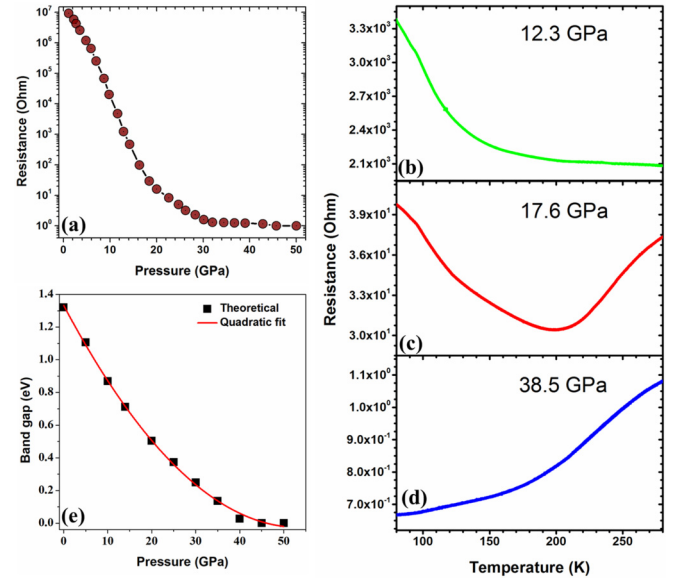

FIG. 4. Electric property measurements and the evolution of band gaps of ReS_2 under high pressure. (a) Electrical resistance of ReS_2 as a function of pressure at room temperature. (b)–(d) The temperature dependence of the resistance of ReS_2 at 12.3, 17.6, and 38.5 GPa, respectively. (e) The calculated pressure-dependent band gap of layered ReS_2. The first two data points calculated from distorted $1T$ phase, others from distorted $1T'$ phase. The band-gap closure is observed at 40 GPa. The band-gap dependence on pressure was fitted using a quadratic function, $E_g = E_0 + aP + bP^2$, where $a = -51$ meV GPa^{-1} and $b = 0.47$ meV GPa^{-2}.

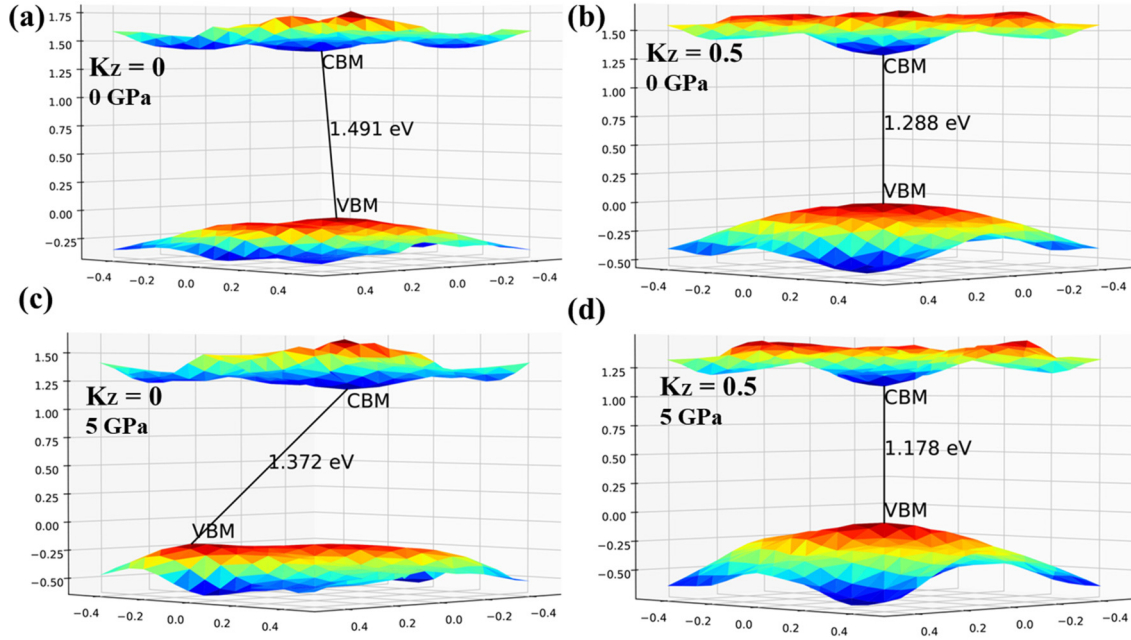FIG. 5. The calculated valence band and conduction band for various models of $1T$-ReS$_2$. (a) $(k_x, k_y, 0)$ at 0 GPa; (b) $(k_x, k_y, 0.5)$ at 0 GPa; (c) $(k_x, k_y, 0)$ at 5 GPa; (d) $(k_x, k_y, 0.5)$ at 5 GPa.

D. Band-structure evolution

It has been claimed that ReS$_2$ has a robust direct band gap regardless of the thickness of materials (from single layer, a few layers, to bulk forms), making ReS$_2$ advantageous over other TMDs for device applications [20,23–27]. However, this was challenged by recent experiments on PL spectra and electrical transport properties that indicated the characteristics of indirect behavior. This controversy was further discussed by several groups recently [55,56]. It has been found that an appreciable interplane interaction results in an experimentally measured difference of 100-200 meV between the valence-band maxima at the Z point (0, 0, 0.5) and the Γ point (0, 0, 0) of the three-dimensional (3D) Brillouin zone [54]. This leads to a direct gap at Z and a close-lying but larger gap at Γ. These

studies indicated that the band structure of $1T$-ReS$_2$ might have a strong dispersion in the 3D reciprocal space, although most of the previous calculations only considered the K-points path based on the hexagonal MoS$_2$, and predicted the gap to be direct at the Γ point. To gain a complete understanding of pressure effects on $1T$-ReS$_2$, we performed the band-structure calculations on $1T$-ReS$_2$ at both 0 and 5 GPa. Figures 5(a) and 5(b) show that the valence-band (VB) and conduction-band (CB) maxima are $(k_x, k_y, 0)$ and $(k_x, k_y, 0.5)$ planes of $1T$-ReS$_2$ at 0 GPa. Clearly, it has an indirect band gap at $(k_x, k_y, 0)$, but the global valence-band maxima (VBM) and conduction-band maxima (CBM) are actually located at (0, 0, 0.5), resulting in a direct band gap of 1.288 eV at the GGA level. This is in quantitative agreement with the previous studies
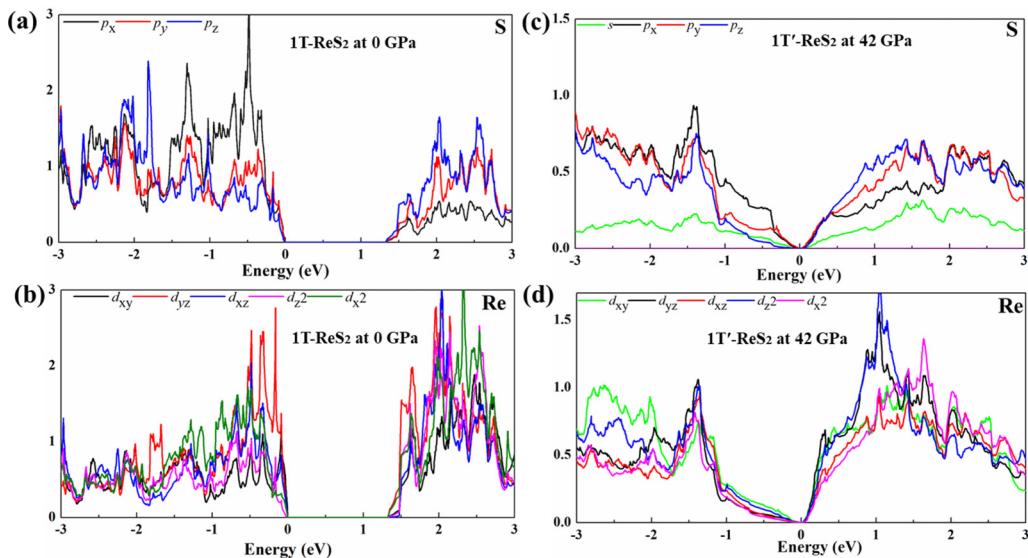

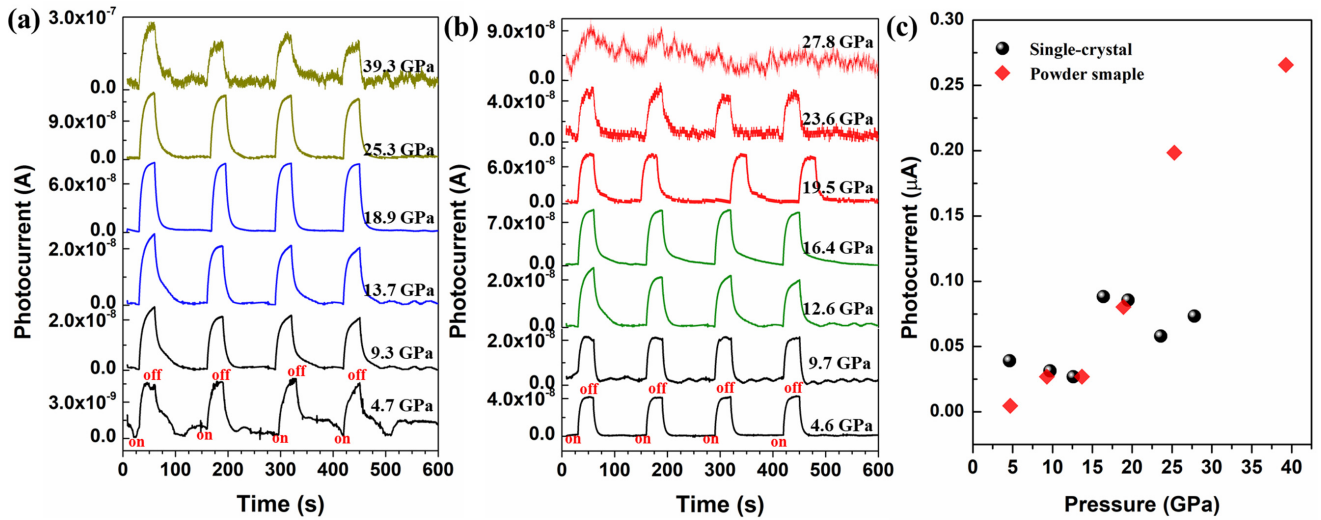FIG. 6. The calculated density of states for (a), (b) distorted-$1T$-ReS$_2$ at 0 GPa; (c), (d) distorted-$1T'$-ReS$_2$ at 65 GPa.

FIG. 7. Photocurrent of (a) bulk ReS_2 sample and (b) single-crystal ReS_2 sample as a function of pressure. The sign of "on" and "off" represent visible-light source switch on and switch off, respectively. (c) Photocurrent–pressure dependence of bulk and single-crystal ReS_2 samples.

[55]. Furthermore, the pressure tends to complicate the band distribution. At 5 GPa, we observed a substantial change of CBM and VBM positions at the $(k_x, k_y, 0)$ plane [Fig. 5(c)], while the changes at the $(k_x, k_y, 0.5)$ plane [Fig. 5(d)] seem barely minimal, making $1T$-ReS_2 a direct semiconductor with a slightly smaller band gap (1.178 eV). However, the global VBM at 5 GPa shifts from $(0, 0, 0.5)$ to the vicinity of $(0, -0.25, 0.25)$, by lowering the energy of $\sim$70 meV. Our results are different from a recent study by Yan *et al.* [32], which studied only a few k-points paths and found $1T$-ReS_2 has an indirect band gap at both ambient and high pressure. This example highlights the complex 3D dispersion features in $1T$-ReS_2, hence a full sampling in the full Brillouin zone is necessary.

In order to obtain more insights, we also computed the angular momentum resolved density of states of distorted-$1T$ phase at 0 GPa and distorted-$1T'$ phase at 42 GPa [Figs. 6(a)–6(d)]. Under compression, the band dispersions of conduction band and valence band have more crossovers due to the broadening of CBM and VBM. Clearly, main contributions to the VBM and the CBM are from hybridized Re-d and S-p states. The Re d_{z^2} orbital's contribution to CBM increases, while the contribution from Re-p orbitals decreases [see Figs. 6(b) and 6(d)]. Likewise, the contribution from S-p_x and S-p_y to CBM decreases with the increase of pressure, while the contribution from S-p_z increases [see Figs. 6(a) and 6(c)]. This is similar to what has been found in MoS_2 in the previous study [25].

E. Visible-light responsiveness measurements

Visible-light harvesting ability for solar energy conversion applications is an important consideration for photovoltaic materials [15,17,19,21,22,36,38]. *In situ* photocurrent measurements of single-crystal and powder semiconducting ReS_2 samples were carried out under high pressure in DAC (Fig. S6) [46]. Both single-crystal and powder ReS_2 samples exhibit typical response to visible light with on-off switch throughout all pressures, as shown in Figs. 7(a) and 7(b). Upon the increase of pressure, the photoresponsiveness of ReS_2 gradually rises,

owing to the continuous decreases in the resistance value and band gap [Fig. 6(c)]. Therefore, the valence electrons are much easier to be excited by visible light and overcome the band gap into CB. Subsequently, photocurrent increases greatly because photoelectron carriers start to migrate quickly and form closed circuit [Fig. 7(c)]. Bulk ReS_2 can still be excited up to 39.3 GPa, indicating that either the sample is semimetal or the semiconducting samples were present due to incomplete electronic transition. More interestingly, the photocurrent signals in single-crystal ReS_2 disappear at 27.8 GPa, which is much lower than that found in bulk ReS_2, presumably attributed to the anisotropic conductivity of single-crystal ReS_2 due to its low lattice symmetry. The successive modulation of the electronic structure and band gap under visible-light irradiation indicates possible pressure-controlled optoelectronics applications of ReS_2.

IV. CONCLUSIONS

In summary, we systematically investigated the structure evolution, electrical transport, vibrational properties, and visible-light responsiveness of ReS_2 under high pressure up to 50 GPa combined with *ab initio* calculations. Both *in situ* XRD and theoretical calculations suggest that ReS_2 undergoes the structural transition at $\sim$7.7 GPa or a lower pressure followed by another semiconductor-metal transition at $\sim$38.5 GPa. Raman spectrum, low-temperature resistivity measurements, and ELF calculation reveal that semiconductor-metal transition of ReS_2 originates from the overlap of the valance and conduction bands due to sulfur-sulfur interlayer sliding as the interlayer spacing decreases upon compression. Lastly, photocurrent measurements indicate a substantial enhancement in visible-light responsiveness of the layered ReS_2 under high pressure.

---

[1] J. A. Wilson and A. D. Yoffe, Adv. Phys. **18**, 193 (1969).

[2] S. Z. Butler, S. M. Hollen, L. Cao, Y. Cui, J. A. Gupta, H. R. Gutiérrez, T. F. Heinz, S. S. Hong, J. Huang, A. F. Ismach, and E. Johnston-Halperin, ACS Nano **7**, 2898 (2013).

[3] Q. H. Wang, K. Kalantar-Zadeh, A. Kis, J. N. Coleman, and M. S. Strano, Nat. Nanotechnol. **7**, 699 (2012).

[4] K. S. Novoselov, D. Jiang, F. Schedin, T. J. Booth, V. V. Khotkevich, S. V. Morozov, and A. K. Geim, Proc. Natl. Acad. Sci. USA **102**, 10451 (2005).

[5] B. Radisavljevic, A. Radenovic, J. Brivio, V. Giacometti, and A. Kis, Nat. Nanotechnol. **6**, 147 (2011).

[6] I. Ferain, C. A. Colinge, and J. Colinge, Nature (London) **479**, 310 (2011).

[7] A. K. Geim and K. S. Novoselov, Nat. Mater. **3**, 183 (2007).

[8] X. Qian, J. Liu, L. Fu, J. Li, and D. Batuk, Science **346**, 1344 (2014).

[9] M. Calandra and F. Mauri, Phys. Rev. Lett. **106**, 196406 (2011).

[10] U. Chatterjee, J. Zhao, M. Iavarone, R. Di Capua, J. P. Castellan, G. Karapetrov, C. D. Malliakas, M. G. Kanatzidis, H. Claus, J. P. C. Ruff, and F. Weber, Nat. Commun. **6**, 6313 (2015).

[11] D. W. Shen, B. P. Xie, J. F. Zhao, L. X. Yang, L. Fang, J. Shi, R. H. He, D. H. Lu, H. H. Wen, and D. L. Feng, Phys. Rev. Lett. **99**, 216404 (2007).

[12] H. Suderow, V. G. Tissen, J. P. Brison, J. L. Martínez, and S. Vieira, Phys. Rev. Lett. **95**, 117006 (2005).

[13] I. Guillamón, H. Suderow, S. Vieira, L. Cario, P. Diener, and P. Rodiere, Phys. Rev. Lett. **101**, 166407 (2008).

[14] Z. Chi, X. Chen, F. Yen, F. Peng, Y. Zhou, J. Zhu, Y. Zhang, X. Liu, C. Lin, S. Chu, Y. Li, J. Zhao, T. Kagayama, Y. Ma, and Z. Yang, Phys. Rev. Lett. **120**, 037002 (2018).

[15] S. Tongay, H. Sahin, C. Ko, A. Luce, W. Fan, K. Liu, J. Zhou, Y. S. Huang, C. H. Ho, J. Yan, and D. F. Ogletree, Nat. Commun. **5**, 3252 (2014).

[16] S. Horzum, D. Çakır, J. Suh, S. Tongay, Y. S. Huang, C. H. Ho, J. Wu, H. Sahin, and F. M. Peeters, Phys. Rev. B **89**, 155433 (2014).

[17] E. Liu, Y. Fu, Y. Wang, Y. Feng, H. Liu, X. Wan, W. Zhou, B. Wang, L. Shao, C. H. Ho, and Y. S. Huang, Nat. Commun. **6**, 6991 (2015).

[18] Y. Feng, W. Zhou, Y. Wang, J. Zhou, E. Liu, Y. Fu, Z. Ni, X. Wu, H. Yuan, F. Miao, B. Wang, X. Wan, and D. Xing, Phys. Rev. B **92**, 054110 (2015).

[19] D. Ovchinnikov, F. Gargiulo, A. Allain, D. J. Pasquier, D. Dumcenco, C. H. Ho, O. V. Yazyev, and A. Kis, Nat. Commun. **7**, 12391 (2016).

[20] D. Zhou, Y. Zhou, C. Pu, X. Chen, P. Lu, X. Wang, C. An, Y. Zhou, F. Miao, C. H. Ho, and J. Sun, NPJ Quantum Mater. **28**, 19 (2017).

[21] M. Rahman, K. Davey, and S. Z. Qiao, Adv. Funct. Mater. **27**, 1606129 (2017).

[22] Q. Zhang, S. Tan, R. G. Mendes, Z. Sun, Y. Chen, X. Kong, Y. Xue, M. H. Rümmeli, X. Wu, S. Chen, and L. Fu, Adv. Mater. **13**, 2616 (2016).

[23] Z. H. Chi, X. M. Zhao, H. Zhang, A. F. Goncharov, S. S. Lobanov, T. Kagayama, M. Sakata, and X. J. Chen, Phys. Rev. Lett. **113**, 036802 (2014).

[24] Z. Zhao, H. Zhang, H. Yuan, S. Wang, Y. Lin, Q. Zeng, G. Xu, Z. Liu, G. K. Solanki, K. D. Patel, and Y. Cui, Nat. Commun. **6**, 7312 (2015).

[25] A. P. Nayak, S. Bhattacharyya, J. Zhu, J. Liu, X. Wu, T. Pandey, C. Jin, A. K. Singh, D. Akinwande, and J. F. Lin, Nat. Commun. **5**, 3731 (2014).

[26] A. P. Nayak, Z. Yuan, B. Cao, J. Liu, J. Wu, S. T. Moran, T. Li, D. Akinwande, C. Jin, and J. F. Lin, ACS Nano **9**, 9117 (2015).

[27] S. Duwal and C. S. Yoo, J. Phys. Chem. C **12**, 5101 (2016).

[28] N. Bandaru, R. S. Kumar, D. Sneed, O. Tschauner, J. Baker, D. Antonio, S. N. Luo, T. Hartmann, Y. Zhao, and R. Venkat, J. Phys. Chem. C **118**, 3230 (2014).

[29] Y. Guo, H. Deng, X. Sun, X. Li, J. Zhao, J. Wu, W. Chu, S. Zhang, H. Pan, X. Zheng, and X. Wu, Adv. Mater. **29**, 1700715 (2017).

[30] D. Hou, Y. Ma, J. Du, J. Yan, C. Ji, and H. Zhu, J. Phys. Chem. Solids **71**, 1571 (2010).

[31] O. B. Aslan, D. A. Chenet, A. M. van der Zande, J. C. Hone, and T. F. Heinz, ACS Photonics **3**, 96 (2015).

[32] Y. Yan, C. Jin, J. Wang, T. Qin, F. Li, K.Wang, Y. Han, and C. Gao, J. Phys. Chem. Lett. **8**, 3648 (2017).

[33] H. K. Mao, J. Xu, and M. Bell, J. Geophys. Res. **91**, 4673 (1986).

[34] A. P. Hammersley, High Press. Res. **14**, 235 (1996).

[35] G. S. Pawley, J. Appl. Crystallogr. **14**, 357 (1981).

[36] X. Lü, W. Yang, Z. Quan, T. Lin, L. Bai, L. Wang, F. Huang, and Y. Zhao, J. Am. Chem. Soc. **136**, 419 (2014).

[37] P. Wang, D. He, L. Wang, Z. Kou, Y. Li, L. Xiong, Q. Hu, C. Xu, L. Lei, Q. Wang, J. Liu, and Y. Zhao, Appl. Phys. Lett. **107**, 101901 (2015).

[38] Y. Wang, X. Lü, W. Yang, T. Wen, L. Yang, X. Ren, L. Wang, Z. Lin, and Y. Zhao, J. Am. Chem. Soc. **137**, 11144 (2015).

[39] A. R. Oganov and C. W. Glass, J. Chem. Phys. **124**, 244704 (2006).

[40] Q. Zhu, D. Y. Jung, A. R. Oganov, C. W. Glass, C. Gatti, and A. O. Lyakhov, Nat. Chem. **5**, 61 (2013).

[41] G. Kresse and J. Furthmuller, Phys. Rev. B **54**, 11169 (1996).

[42] J. P. Perdew, K. Burke, and M. Ernzerhof, Phys. Rev. Lett. **77**, 3865 (1996).

[43] P. E. Blochl, Phys. Rev. B **50**, 17953 (1994).

[44] H. H. Murray, S. P. Kelty, R. R. Chianelli, and C. S. Day, Inorg. Chem. **33**, 4418 (1994).

[45] H. J. Lamfers, A. Meetsma, G. A. Wiegers, and J. L. De Boer, J. Alloys Compd. **241**, 34 (1996).

[46] See Supplemental Material at http://link.aps.org/supplemental/10.1103/PhysRevB.97.235202 for crystal structure and pressure dependence of lattice parameters of layered ReS$_2$, enthalpy curve as a function of pressure, schematics of electrical resistance measurements in DAC, and electrical resistance results using large volume press.

[47] F. Birch, J. Geophys. Res. **83**, 1257 (1978).

[48] D. L. Heinz and R. Jeanloz, J. Appl. Phys. **55**, 885 (1984).

[49] E. Soignard, O. Shebanova, and P. F. McMillan, Phys. Rev. B **75**, 014104 (2007).

[50] K. Woodhead, S. Pascarelli, A. L. Hector, R. Briggs, N. Alderman, and P. F. McMillan, Dalton Trans. **43**, 9647 (2014).

[51] A. Salamat, R. Briggs, P. Bouvier, S. Petitgirard, A. Dewaele, M. E. Cutler, F. Corà, D. Daisenberger, G. Garbarino, and P. F. McMillan, Phys. Rev. B **88**, 104104 (2013).

[52] M. Blanchard, K. Wright, J. D. Gale, and C. R. A. Catlow, J. Phys. Chem. C **111**, 11390 (2007).

[53] A. K. Kleppe and A. P. Jephcoat, Mineral. Mag. **68**, 433 (2004).

[54] A. Savin, R. Nesper, S. Wengert, and T. Fässler, Angew. Chem., Int. Ed. Engl. **36**, 1808 (1997).

[55] J. L. Webb, L. S. Hart, D. Wolverson, C. Chen, J. Avila, and M. C. Asensio, Phys. Rev. B **96**, 115205 (2017).

[56] D. Biswas, A. M. Ganose, R. Yano, J. M. Riley, L. Bawden, O. J. Clark, J. Feng, L. Collins-Mcintyre, M. T. Sajjad, W. Meevasana, T. K. Kim, M. Hoesch, J. E. Rault, T. Sasagawa, D. O. Scanlon, and P. D. C. King, Phys. Rev. B **96**, 085205 (2017).